Local structural mechanism for enhanced energy storage properties in heterovalent doped NaNbO₃ ceramics

Cho Sandar Htet [a], Alicia Maria Manjón-Sanz [b], Jue Liu [b], Chaimae Babori [c,d], Mahmoud Barati [c,d], Frederick P. Marlton [e], Laurent Daniel [c,d], Mads Ry Vogel Jørgensen [f,g], Abhijit Pramanick [a,c,d,h,*]

[a] Department of Materials Science and Engineering, City University of Hong Kong, Hong Kong, China
[b] Neutrons Scattering Division, Oak Ridge National Laboratory, Oak Ridge, TN 37831, USA
[c] Group of Electrical and Electronic Engineers, Paris, University Paris-Saclay, Gif-sur-Yvette, France
[d] Sorbonne Université, CNRS, Laboratoire de Génie Electrique et Electronique de Paris, 75252 Paris, France
[e] School of Mathematical and Physical Sciences, University of technology, Sydney, NSW, Australia
[f] Department of Chemistry and iNANO, Aarhus University, 8000 Aarhus C, Denmark
[g] MAX IV Laboratory, Lund University, SE-221 00 Lund, Sweden
[h] Center for Neutron Scattering, City University of Hong Kong, Hong Kong, China

ABSTRACT

In recent years, there is a growing interest for new lead-free oxides with reversible antiferroelectric (AFE)-ferroelectric (FE) phase transition for high-power energy-storage applications. NaNbO₃-based ceramics are particularly attractive due to their easy synthesis and cost-effectiveness. In order to stabilize reversible AFE-FE phase transition, NaNbO₃ is doped with a combination of heterovalent substitutions, although the underlying structural mechanism for the same is poorly understood. Here, we investigated local and average structures of Ca/Zr doped NaNbO₃ using neutron total scattering. We show that Ca/Zr doping increases the average AFE phase ($Pbma$) fraction, however, the material remains as a composite of both FE ($P2_1ma$) and AFE regions. Analysis of local structure suggests that increase in the long-range AFE phase results from more extensive twinning of local FE regions, due to introduced charge disorder. We propose that enhanced energy-storage properties of Ca/Zr-doped NaNbO₃ arises from localized twin boundary motion between the defect-induced pinning centers.

1. Introduction

Materials for high-power energy storage constitute vital passive components in advanced power electronics devices that require fast switching and higher energy efficiency, such as to achieve improved power quality in electric/hybrid vehicles and in electric grids. Ceramic capacitors made with antiferroelectrics are of particular interest for this purpose due to their capability to operate under high voltage, high transient currents, and greater reliability [1–4]. The concept of anti-ferroelectricity was first proposed by Kittel et al. in 1951. Antiferroelectric materials have two sublattices that polarize in opposite directions and therefore results in an overall net zero polarization [5]. Macroscopically, AFE materials exhibit large electric-field induced saturation polarization and near-zero remanent polarization at zero electric field, which leads to their large energy storage properties. In

recent years, there has been growing interest in lead-free AFE materials such as AgNbO₃ and NaNbO₃ due to the potential adverse environmental and health effects of Pb-based antiferroelectrics, such as PbZrO₃. Among AFE materials, NaNbO₃ is particularly promising because of its high energy density and ease of sample preparation. At room temperature, pure NaNbO₃ can show a coexistence of both AFE P ($Pbma$) and FE Q ($P2_1ma$) phases. It is remarkable that small amounts of dopants can significantly change the AFE and FE phase fractions in NaNbO₃. For example, less than 2% substitution of K or Li for Na increases the average phase FE fraction by 95% and 85%, respectively [6,7]. In contrast, the introduction of CaZrO₃, SrZrO₃, SrSnO₃, CaSnO₃ and CaHfO₃ into NaNbO₃ leads to an increase in the stability of AFE phase [8–13]. Doping induced changes in FE/AFE phase fractions was initially attributed to changes in the average tolerance factor [11]. However, recent studies indicate that the tolerance factor cannot be the only deciding factor for

---

controlling the AFE/FE phase composition in doped NaNbO$_3$ ceramics [6,14].

Based on a comparison of long-range average and local atomic structures, we rationalized such behavior based on the extent of 180° twinning, whereby the bulk of a twin variant constitutes an FE phase whereas the twin boundary region constitutes an AFE phase [6]. In other words, the average AFE phase is promoted by more extensive 180° twinning and vice-versa. Furthermore, we ascertained that the extent of twinning is determined by a competition between the long-range polarizing field and local atomic distortions, which is subjected to change by doping. For (K,Na)NbO$_3$ ceramics, the substitution of Na with isovalent K reduces the A-site distortion and consequently decreases the extent of twinning, thereby decreasing the AFE phase fraction [6]. In contrast, recent studies indicated that addition of a few atomic% of heterovalent dopants, such as Ca/Zr, promotes the AFE phase [11,15, 16]. Here, we show that while Ca/Zr doping of NaNbO$_3$ does indeed increases the volume fraction of the average AFE phase, the local structure is still better described by the FE $P2_1ma$ structural model. We argue that the apparent increase in the average AFE phase fraction is due to a more extensive local twinning, which results from introduction of additional charge disorder and hence a weakening of the long-range polarizing field of the B-site distortions. The observed pinching of the macroscopic polarization-electric field hysteresis loops in Ca/Zr-doped NaNbO$_3$ is proposed to be due to localized motion of twin boundaries between the defect-induced pinning centers. Our study indicates that introduction of charge disorder and local pinning of twin boundaries, rather than changes in the local structure, are the most important factors towards improving the energy-storage properties of heterovalent doped NaNbO$_3$ ceramics.

2. Experimental method

Ceramic samples of (1-x)(NaNbO$_3$)-x(CaZrO$_3$), where x = 0.02, 0.04 and 0.06, denoted as NNCZ2, NNCZ4 and NNCZ6, respectively, were prepared by the conventional solid-state reaction method. Details of sample preparation method are included in the SI. Representative scanning electron micrographs of fracture surfaces of the prepared ceramics for composition NNCZ4 are shown in Fig. 1. Both transgranular and intergranular fractures surfaces were observed, such as see Fig. 1(a, b). The microstructures of the ceramics showed dense packing of the grains with well-formed grain boundaries. The grain sizes are approximately in the range of 5–10 μm. The polyhedral nature of the grains is evident from the Fig. 1(c), clearly showing the {111} (hexagonal) and {001} (square) crystal faces, which is based on a reasonable assumption of truncated octahedral shape of the sintered grains [17].

The ceramic pellet samples of each composition were used for the measurement of polarization-electric field hysteresis loops. The schematic of the measurement bench used for dielectric displacement measurements is shown in Fig. 2(a). This experimental setup is designed to apply an electric field up to 20 kV to the sample, to measure the induced electric displacement [18]. The sample is placed between two fixtures, electrically isolated using Teflon parts and immersed in a PTFE container filled with insulating fluid to prevent dielectric breakdown. The upper electrode is accessed using a low-stiffness spring such that the contact between the spring and the sample is ensured and spring-induced stress can be neglected. The electric field E is produced by a high voltage amplifier (Trek 20/20 C-HS) and controlled by a real time Dspace hardware module with a maximum sampling frequency of 5 kHz. The dielectric displacement D is measured from the upper electrode of the sample using the conditioner with an operational amplifier integrator circuit shown in Fig. 2(b) (with an integrating capacitor of 2057 nF). The sample can be connected with the operational amplifier integrator circuit via the BNC IN socket. The output voltage is acquired from the BNC OUT socket. The two diodes D1 and D2 are used to protect
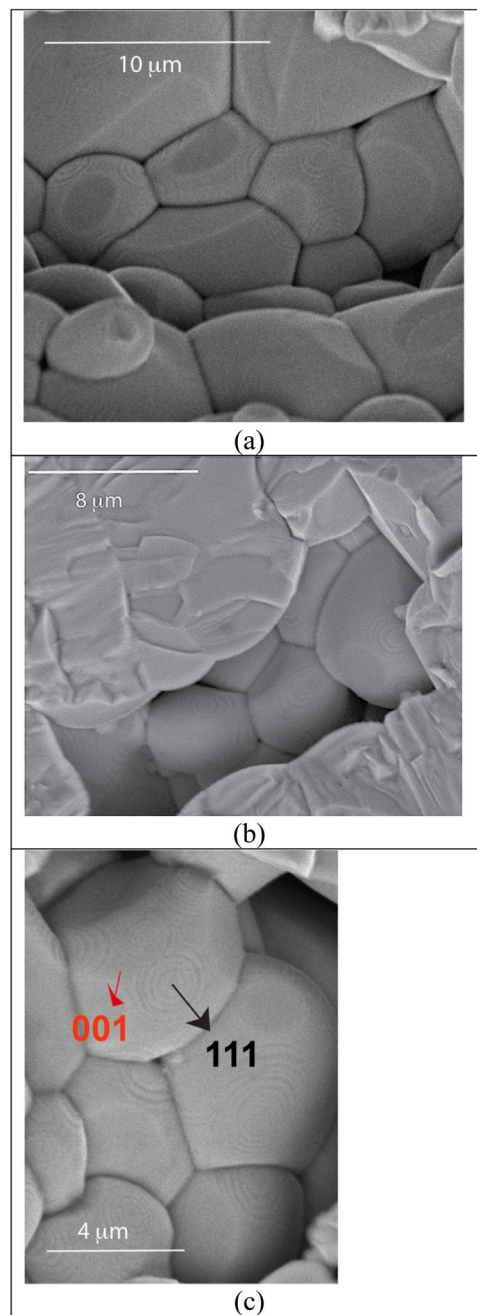
Fig. 1. (a,b) Representative micrographs of fracture surfaces of Ca/Zr-doped NaNbO$_3$ ceramics. (c) The (111) and (001) crystal faces of the grains are marked in this micrograph.

the circuit from overvoltage. Capacitors C1 to C3 correspond to three measurement ranges. The output of this circuit has been adapted to give a range of 0–10 V. The measurements are recorded using the Dspace hardware module. The longitudinal elongation of the sample is measured by the LK-G10 laser CCD displacement sensor connected to the Keyence LK-GD500 conditioner. For this purpose, the sensor is positioned above the sample and rigidly attached to the slider.

For structural measurements, the ceramics were ground using a mortar and pestle and then sieved to obtain relative uniform particle size. The time-of-flight neutron scattering measurements using the powdered ceramic samples were conducted at the POWGEN instrument of the Spallation Neutron Source at the Oak Ridge National Lab [19].
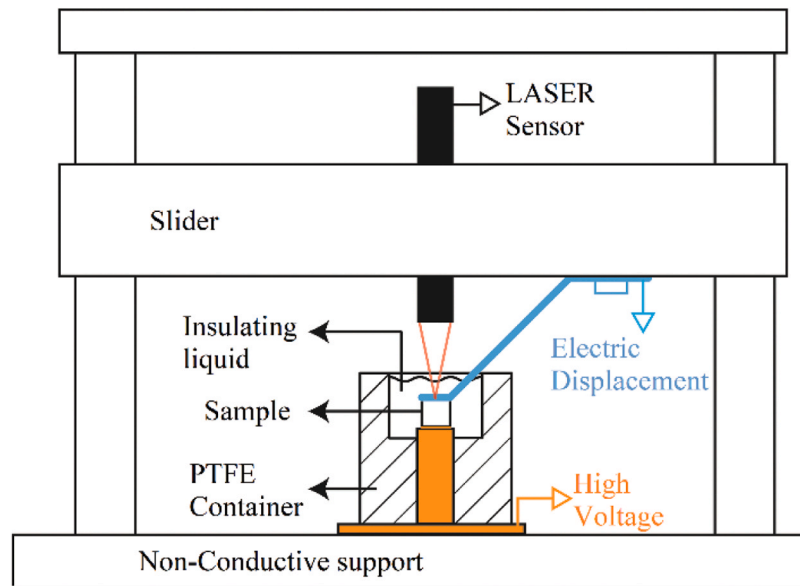
(a)
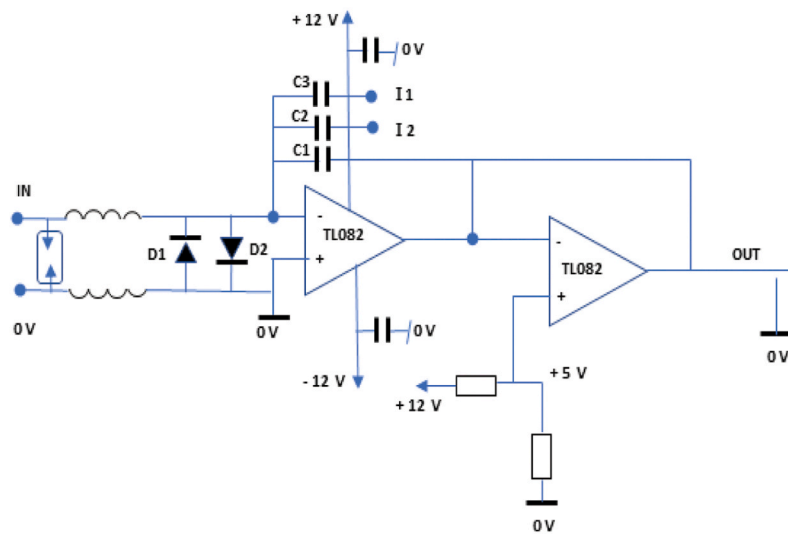
(b)

Fig. 2. (a) Schematic of the measurement bench for measurement of P-E hysteresis [18] (b) the electric displacement measurement circuit.
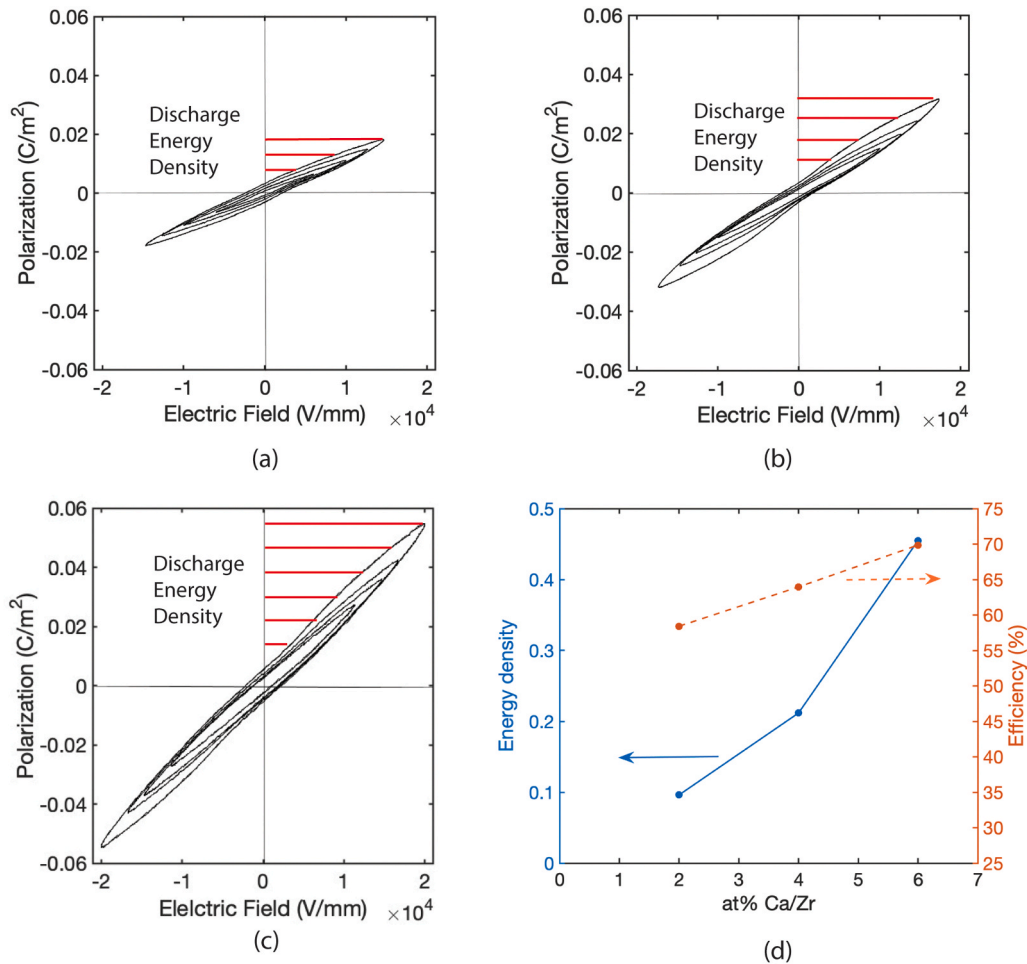
Fig. 3. Polarization-electric field (P-E) hysteresis loops of (a) NNCZ2, (b) NNCZ4 and (c) NNCZ6 ceramics. (d) Energy density and efficiency of the NNCZ ceramics as a function of composition.

Approximately 5 g of powder samples of each composition were sealed in separate 6 mm diameter vanadium cans with helium exchange gas and loaded in the POWGEN automatic changer. The measurement time for each composition was approximately 2 h. A central wavelength of 0.8 Å was used, which covers a d-spacing range of 0.16 – 6.77 Å for diffraction measurements. In order to subtract the background intensity, the scattering pattern on empty vanadium can was taken. The background-corrected intensity was subsequently normalized against proton charge and scattering from a 6-mm vanadium rod to correct for neutron flux and detector efficiency.

3. Results and discussions

3.1. Polarization-electric field (P-E) hysteresis

The macroscopic electrical properties of the ceramics NNCZ2, NNCZ4 and NNCZ6 were characterized from the polarization-electric field (P-E) hysteresis loops, as shown in Fig. 3(a-c). With increasing percentage of Ca/Zr, such as for 4 and 6 at% Ca/Zr, the P-E loops develop a pinched character near zero electric field. Such pinched nature of the P-E loops could indicate an AFE-like behavior. The P-E loops also become slimmer with increasing Ca/Zr addition. The charging and discharging energy density (W_{rec}) of a capacitor can be characterized from its P-E loop using the following equation:

$$W_{rec} = \int_{P_r}^{P_{max}} E dP \tag{1}$$

The discharge energy density is numerically equal to the area enclosed between the polarization curve upon discharging and the vertical polarization axis, as depicted in Fig. 3(a-c) with red lines. The energy efficiency (η) of the capacitor during the charge-discharge process is obtained by the following equation:

$$\eta = \frac{W_{rec}}{W_{total}} \times 100\% \tag{2}$$

where, W_{total}, P_{max}, P_r and E are the total energy storage density, maximum polarization, remnant polarization and applied electric field, respectively.

The variation in the discharge energy density and efficiency of the ceramics as a function of Ca/Zr content is depicted in Fig. 3(d). Both the quantities steadily increase with Ca/Zr content, which can be attributed to development of a pinched character and slimming of the P-E loops. Our results are comparable to those reported in ref. [16] for energy storage properties of NaNbO$_3$ doped with minor amounts of Ca/Zr. For a fundamental understanding of the origins of enhanced energy-storage properties of Ca/Zr-doped NaNbO$_3$ ceramics, we undertook their detailed structural characterization as described below.

3.2. Average structure analysis

The composition-dependent change in the average structure of NNCZ ceramic powder was analyzed from Rietveld refinement of the Bragg diffraction data using the GSAS II software [20]. The full neutron diffraction patterns for NN, NNCZ2, NNCZ4 and NNCZ6 powders that
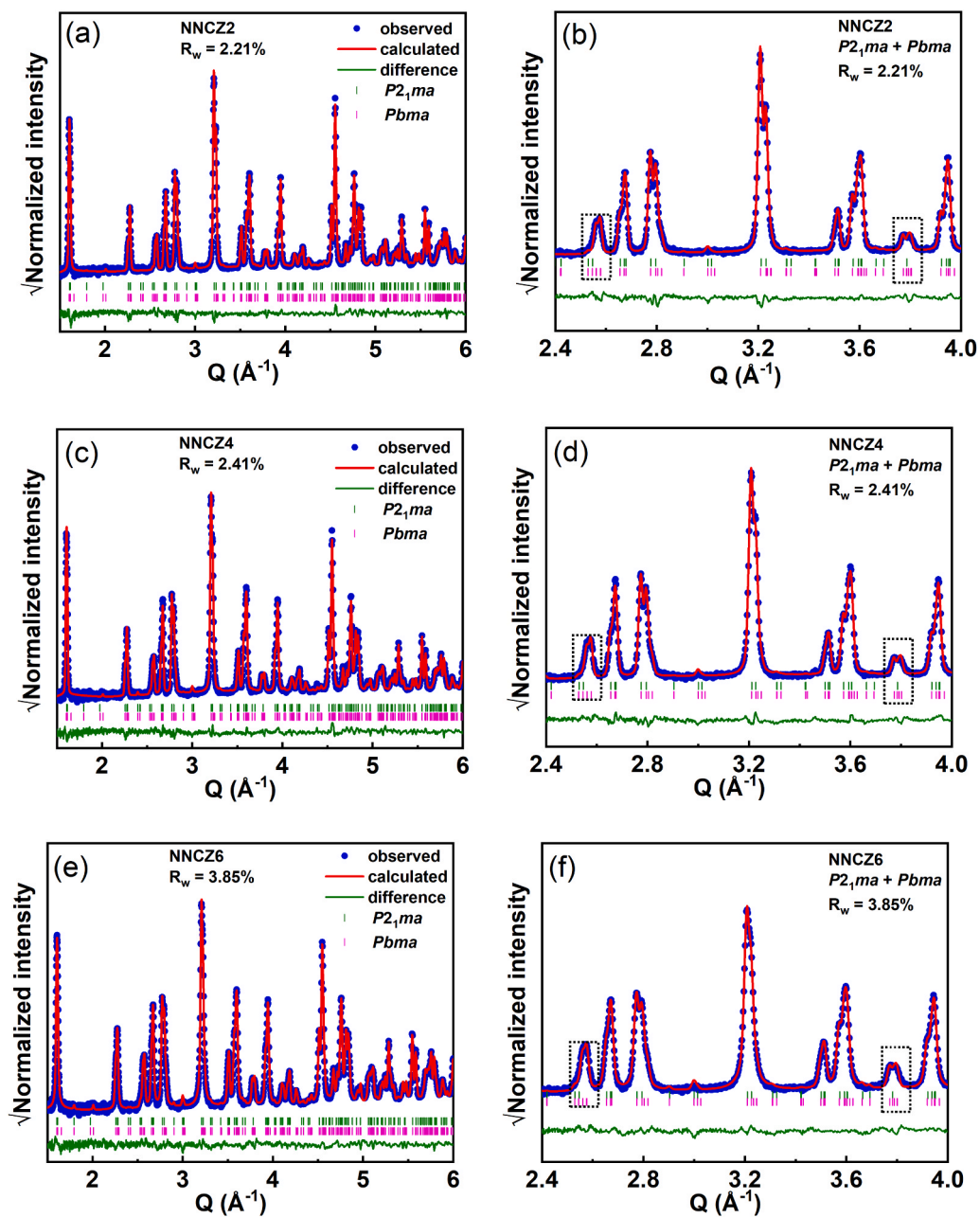
Fig. 4. Rietveld refinement of (1-x)NaNbO$_3$-xCaZrO$_3$ at room temperature. NNCZ2, NNCZ4, and NNCZ6 refer to x = 0.02, 0.04, and 0.06, respectively: (a,b) NNCZ2 (c,d) NNCZ4 (e,f) NNCZ6. The superlattice reflections (with respect to pseudocubic unit cell) present in the region of Q = 2.4–4.0 Å^{-1} are shown with black rectangle boxes. Observed (blue symbols), calculated (red line), difference (green line) profiles, and Bragg positions (green and pink ticks) obtained after the Rietveld refinement using GSAS II software. Weighted residuals (R$_w$) are shown for all the refinements.
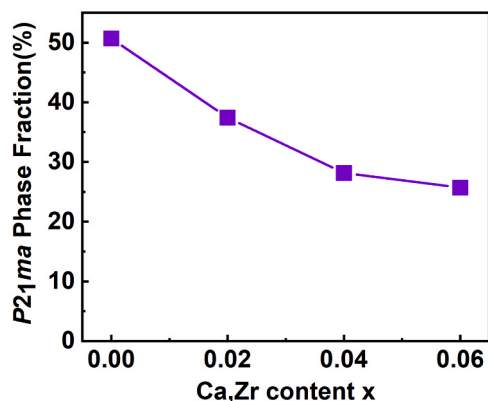
Fig. 5. Phase fraction of $P2_1ma$ (Q phase) in $(1-x)NaNbO_3-xCaZrO_3$ as a function of composition. $NaNbO_3$ data are obtained from ref [22].

are obtained from POWGEN instrument are shown in Fig. S1(a) in the Supplementary Information (SI). The superlattice (SL) peaks at Q = 2.4 and 4 Å^{-1} are presented in Fig. S1(b) with rectangular boxes, indicating the regions corresponding to SL peaks labelled as SL1 and SL2, respectively. Fig. 4(a,c,e) depicts the Rietveld refinement fits of the neutron diffraction patterns of NNCZ powder samples as a function of composition. The Bragg diffraction patterns appears similar for all the measured compositions, except for small changes in the superlattice (SL) peaks at Q = 2.45 and 3.8 Å^{-1}, which are highlighted in the Fig. 4(b,d,f). Note that the highlighted peaks refer to as SL peaks with reference to the cubic perovskite structure and arise due to specific long-range ordering of octahedral tilting patterns [21,22]. In order to fit the measured diffraction data for quantitative phase analysis, we tried the structural models of orthorhombic *Pbma* and $P2_1ma$, which correspond to the AFE and FE phases, respectively. The starting structural parameters for refinement were taken from our recent study on the structural analysis of $NaNbO_3$ [22]. The structural parameters, viz., unit cell constants, atomic coordinates, atomic displacement parameters (ADPs), background coefficient, and sample-related peak profile parameters, were refined to best fit the experimental Bragg diffraction data. The quality of the fits were assessed visually and from the values of the weight residuals R_w [23]. Similar to our earlier report on $NaNbO_3$ [22], we observe here that a two-phase mixture of $P2_1ma$ + *Pbma* provides the best fit to the diffraction data for all the measured compositions, as compared to either single-phase $P2_1ma$ or *Pbma* models (see Figs. S2, S3 and S4 in the SI). The results of the structural parameters obtained from the Rietveld refinement of the powder neutron diffraction data are listed in the Table S1 in the SI. Fig. 5 shows change in phase fraction of the orthorhombic $P2_1ma$ phase as a function of composition. With the incorporation of Ca/Zr, the $P2_1ma$ phase fraction steadily decreases from ~50% in pure NN to ~25% for NNCZ6, indicating a stabilization of the *Pbma* phase. However, in contrast to earlier studies, quantitative evaluation from high-resolution neutron diffraction data here shows that addition of Ca/Zr does not completely transform the *FE* phase regions to an *AFE* phase and the materials remains as a composite of both FE and AFE phases. This emphasizes that assessment of FE-to-AFE transformation should not be based on the appearance of a pinched P-E hysteresis loop alone.

The evolution of the AFE/FE phase fractions with composition can be further gauged from the subtle changes in the SL peak appearances, such as shown in Fig. 6. Note that the *hkl* indices in Fig. 6 refer to regular reflections from the *Pbma* and the $P2_1ma$ crystal lattices, but can be referred to as SL reflections with regard to the simple cubic perovskite structure. This is since the unit cells of the Q and P phases are doubled and quadrupled along the [010] direction in reference to the pseudocubic perovskite lattice, respectively, which gives rise to SL diffraction peaks with $n/2\{0k0\}_{cubic}$-type for the Q phase and $n/4\{0k0\}_{cubic}$-type

for the *P* phase. Consequently, some peaks appear exclusively in the *P* phase such as (2 3 0), which refer to the $(1 \frac{3}{4} 1)_{cubic}$ SL reflection, but are absent in the *Q* phase. Similarly, some of the peaks appear identical for both the structures, such as (1 0 2)/(2 0 1); while some other peaks appear coincidental for the two structures but with different *hkl* indices, such as (0 2 3) for the *Q* phase and (0 4 3) for the *P* phase. These features in the SL peaks help to identify visually the trends for the changes in AFE/FE volume fractions, as explained in [6]. Here, we observe an increase in the spectral weight of SL reflections at higher Q values in the range of Q ~ 2.5–2.6 Å^{-1}, and a sharpening of the split peaks in the region of Q ~ 3.7–3.85 Å^{-1}, with increase in Ca/Zr content – these trends provide visual evidence of an increase in the volume fraction of the average *P* phase with *Pbma* space group (or decrease in volume fraction of the *Q* phase with $P2_1ma$ space group), which is consistent with the result depicted in Fig. 5.

3.3. Local structural analysis

In order to examine the local structural origin of changes in the volume fractions of AFE/FE phases with addition of heterovalent Ca/Zr dopants in $NaNbO_3$, we undertook their neutron pair distribution function (PDF) and Raman scattering analyses.

3.3.1. Neutron pair distribution function analysis

For PDF analysis, the measured total scattering intensities from POWGEN (Bragg + diffuse scattering) were normalized and reduced to obtain the structure function S(Q), where Q is the scattering vector (see in Fig. S5 in the SI). The PDF G(r) was obtained using the equation:

$$G(r) = \left(\frac{2}{\pi}\right) \int_{Q_{min}}^{Q_{max}} Q(S(Q) - 1)\sin(Qr)dQ \qquad (3)$$

where G(r) is related to the atom-pair density function $\rho(r)$ and the pair density function g(r) through the following relations:

$$G(r) = 4\pi r[\rho(r) - \rho_0] = 4\pi r\rho_0[g(r) - 1] \qquad (4)$$

where ρ_0 is the atomic number density [24,25]. In the above equations, we used a Q_{min} of 0.5 Å^{-1} and Q_{max} of 25 Å^{-1}. It is worth noting that the measured scattering function was not absolutely normalized according to the sample number density. Instead, it is scaled according to the ratio of the normalized scattering power between vanadium rod and sample at Q_{max} of 25 Å^{-1}. Also, the small-angle scattering intensity below Q_{min} was excluded in the Fourier transformation process.

Fig. 7 illustrates the composition-dependent *G(r)* of NNCZ ceramic powders in the range of r < 4 Å, which indicates the nearest neighbour and next nearest neighbour correlations that are highlighted by arrows. The first two peaks at r ~1.9 Å and ~2.1 Å correspond to the Nb/Zr-O (B-O) interatomic correlations. The splitting of the B-O peak indicates that the Nb/Zr are off-centered within the oxygen octahedra. The peak at r ~ 2.8 Å is contributed from both O-O and A-O interatomic correlations. The two shoulders at r ~ 2.45 Å and r ~ 3.2 Å indicates a split in the Na/Ca-O (A-O) interatomic correlations, which could be due to the oxygen octahedral tilting and/or the off-centering of the A-site atoms within the oxygen dodecahedron. To quantify the local off-centering displacements of the A and B-sites, the PDFs were analyzed using the program PDFGui [26]. The fitting of *G(r)* was initiated with the starting parameters obtained from the corresponding Rietveld refinement of the Bragg diffraction data. The refinement process involved the optimization of several structural parameters, including the scale factor, unit cell parameters, atomic positions, and atomic displacement parameters (ADPs), to achieve the best fit to the experimental data. We used two different models *Pbma* and $P2_1ma$, to fit the *G(r)* data. Note that the unit cell dimensions of $P2_1ma$ and *Pbma* are different, with $P2_1ma$ having a smaller unit cell dimension of b ~8 Å and *Pbma* having a longer unit cell dimension of b ~16 Å. Considering that any particular structural model should fit the measured PDF over at least one unit cell, we examined the
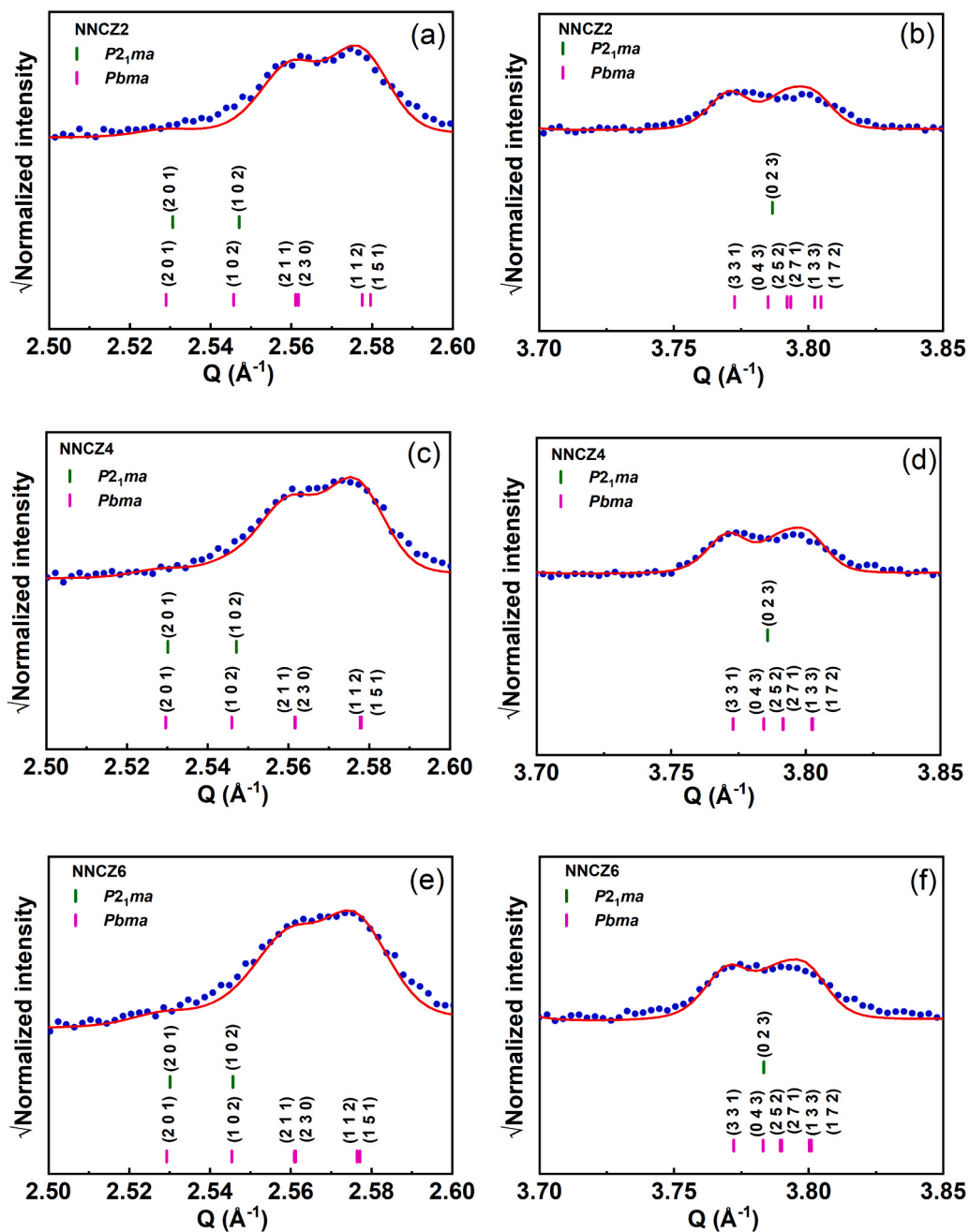
Fig. 6. The refined superlattice reflections (with respect to pseudocubic unit cell) present in the region of Q = 2.5–3.85 Å^{-1} are shown in the enlarged view; (a,b) NNCZ2, (c,d) NNCZ4, and (e,f) NNCZ6, respectively. Observed (blue symbols), calculated (red line), difference (green line) profiles, and Bragg positions (green and pink ticks) are shown. Scales are kept the same for comparison.
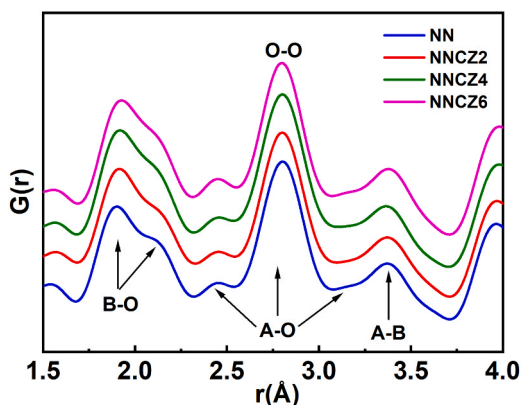
Fig. 7. Neutron pair distribution function G(r) of(1-x)NaNbO$_3$-xCaZrO$_3$ in the range of $r \sim$ 1.5–4 Å. NN, NNCZ2, NNCZ4, and NNCZ6 refer to x = 0, 0.02, 0.04, and 0.06, respectively.

corresponding fits for the *Pbma* and *P*2$_1$*ma* models over different *r* values in the range of $r \sim$ 1.7 − 16 Å.

The use of the *Pbma* model to fit the observed G(r) over *r* ~1.7–16 Å yielded a reasonable fit for NNCZ2, as shown in Fig. 8(a). However, agreement to the measured data is markedly different over different ranges of interatomic distances: the *Pbma* model provided a better fit to the *G*(r) data at larger distances *r* > 8 Å (R$_w$ ~ 8.67%) as compared to that at shorter distance of r < 8 Å (R$_w$ ~ 15.06%), as shown in Fig. 8(a). Instead, if the *P*2$_1$*ma* model is used to fit the measured *G*(*r*) over *r* ~ 1.7–8 Å, it provides a better fit with a lower R$_w$ ~ 12.32%, as shown in Fig. 8(b). However, if the *P*2$_1$*ma* model is projected over longer distances of *r* > 8 Å, the agreement between the calculated and the measured data becomes progressively worse. Indeed, examination of the nearest neighbor B-O and A-O correlations clearly demonstrates better agreement for the *P*2$_1$*ma* model over the *Pbma* model (see SI, Fig. S6) Similar results are also observed for NNCZ4 and NNCZ6, as shown in Figs. 8(c,d) and 8(e,f), respectively. Based on these results, it is apparent that the *P*2$_1$*ma* model is better suited to describe the nearest and next-nearest neighbour interatomic correlations in NNCZ samples, while the longer range structure is closer to the AFE *Pbma* model.

3.3.2. Raman scattering results

Further to the neutron PDF, the local structure was also examined from Raman scattering measurements. Raman spectroscopy is an effective technique for characterizing the local structural distortions in perovskite ferroelectrics by examining the shifts in frequency and broadening of Raman peaks. Fig. 9 shows the Raman spectra of pure NN and NNCZ samples at room temperature. We can observe an overall similarity in the Raman spectra for all the compositions, which indicates that the local atomic environment remains similar even with 6 at% Ca/Zr doping. For closer examination, the different peaks in the Raman scattering spectra can be assigned to particular vibrational modes based on group theory. Earlier studies have categorized the ν_1, ν_2, ν_3, and ν_4 modes as stretching modes, while the remaining modes are associated with bending modes [8,27–29]. Specifically, the Raman modes below 160 cm^{-1} originate from translational motion of the Na$^+$/Ca^{2+} cations [28]. The peaks between 160 and 400 cm^{-1} can be attributed to B-O bending vibration modes and are assigned as ν_5 and ν_6. The high-frequency vibrational modes between 400 and 750 cm^{-1} can be attributed to the O-B-O stretching mode and are assigned as ν_1, ν_2, ν_3, and ν_4. Some small changes in the Raman spectra can be observed as a function of composition. For example, we notice changes in the relative intensities for the peaks attributed to the bending modes at 256 cm^{-1} (ν_5^2) and 278 cm^{-1}(ν_5^1), as shown in Fig. 9(c); these could arise due to changes in distortions of BO$_6$ octahedra resulting from the displacement of B-site atoms [12,16]. Similarly, we can observe peak broadening in

the range of 160–750 cm^{-1} with increase doping content. Such broadening can be caused by addition of Zr^{4+}, which can influence the vibrational energy for the bending and stretching modes locally due to differences in ionic size between Zr^{4+} (0.72 Å) and Nb^{5+} (0.64 Å). However, in order to examine whether the local structural symmetry undergoes any change with Ca/Zr, we should examine some specific features in the spectra. Interestingly, the intensity of 125 cm^{-1}, which was initially observed in all compositions, decreases and broaden as the Ca/Zr content increases, as shown in Fig. 9(b). This decrease in intensity may indicate a reduction of Q phase [27,30]. However, we did not observe the emergence of a peak at 96 cm^{-1}, which was earlier related to the *Pbma* symmetry [27]. These features support the conclusion drawn from the neutron *G*(*r*) measurements that there is no conclusive evidence to indicate a phase change from *P*2$_1$*ma* to *Pbma* for the local structure.

4. Discussion

4.1. Comparison of local and average structures

A better understanding of the FE and AFE structures in NaNbO$_3$ solid-solutions can be obtained from comparing the atomic positions in the two different structures. Fig. 10(a-b) illustrates the crystal structures of AFE *P* (*Pbma*) and FE *Q* phase (*P*2$_1$*ma*). The unit cell of the AFE phase consists of four octahedral layers along the *b*-axis, labeled as Layers 1–4 in Fig. 10(a). Instead, the unit cell of the FE phase consists of two octahedral layers along the *b*-axis. Therefore, one can consider that the structure of the AFE *P* phase may be obtained by stacking two 180° twin variants of the FE *Q* phase along the *b*-axis, as shown in Fig. 10(b). However, this needs to be verified from the characteristic atomic displacements in the two different structures. In Fig. 10(a), the unique positions of the Na atoms in the *Pbma* crystal structure are labeled as Na1 and Na2. For the 180° twin variants of the *P*2$_1$*ma* structure shown in Fig. 10(b), the displacements of the Na atoms labelled as A-D should be compared to those of the Na1/Na2 atoms in the average *Pbma* structure. That is, for the twin model to be correct the average displacement of the NaA and NaB (or NaC and NaD) atoms within the local *P*2$_1$*ma* twin variants must approach to that of the Na1 (or Na2) atoms in the average *Pbma* structure. Fig. 11 shows the A/B-site off-centering displacements and the octahedral distortions for the different layers in the *Pbma* and *P*2$_1$*ma* structures in detail. For the *Pbma* structure, the Na1 atoms are not displaced with respect to the center of their surrounding O atoms, whereas the Na2 atoms undergo displacement along the [100] direction in the layer 2, and along the [$\bar{1}$00] direction in the layer 4 (Fig. 11(a-d)). In comparison, for the *P*2$_1$*ma* structure of twin variant 1, the NaA (or NaC) atoms undergo displacement along the [101] direction, while the NaB (or NaD) atoms displace along the [10$\bar{1}$] direction (Fig. 11(e-h)). This can be explained as follows: the average of the individual displacements of the NaC and NaD atoms in the twin variant 1 is consistent with a net displacement along the [100] direction for the Na2 atom, which is preserved in the layer 2 of the average *Pbma* structure. Similarly, the average of the individual displacements of the NaC and NaD atoms in the twin variant 2 is consistent with a net displacement along the [$\bar{1}$00] direction for the Na2 atom in layer 4 of the average *Pbma* structure. As illustrated in Fig. 10(b), the position of Na1 constitutes a region overlapped between the two local 180° twin variants; consequently, Na1 appears to have a net zero displacement in the average *Pbma* structure. Nevertheless, Na1 has a higher U$_{iso}$ in the average structure as compared to other atomic sites, which indicates greater disorder for this site (see Table S1 in SI). A visual representation of the comparable atomic displacements in the two structures is provided in the polar plot in Fig. 12, which illustrates the relationship between the Na atom displacements in both the average and local structures. In the local *Q* phase, the Na atom displace along both [101] and [10$\bar{1}$] in the a-c plane. Therefore, the average of Na local displacements in the *P*2$_1$*ma*
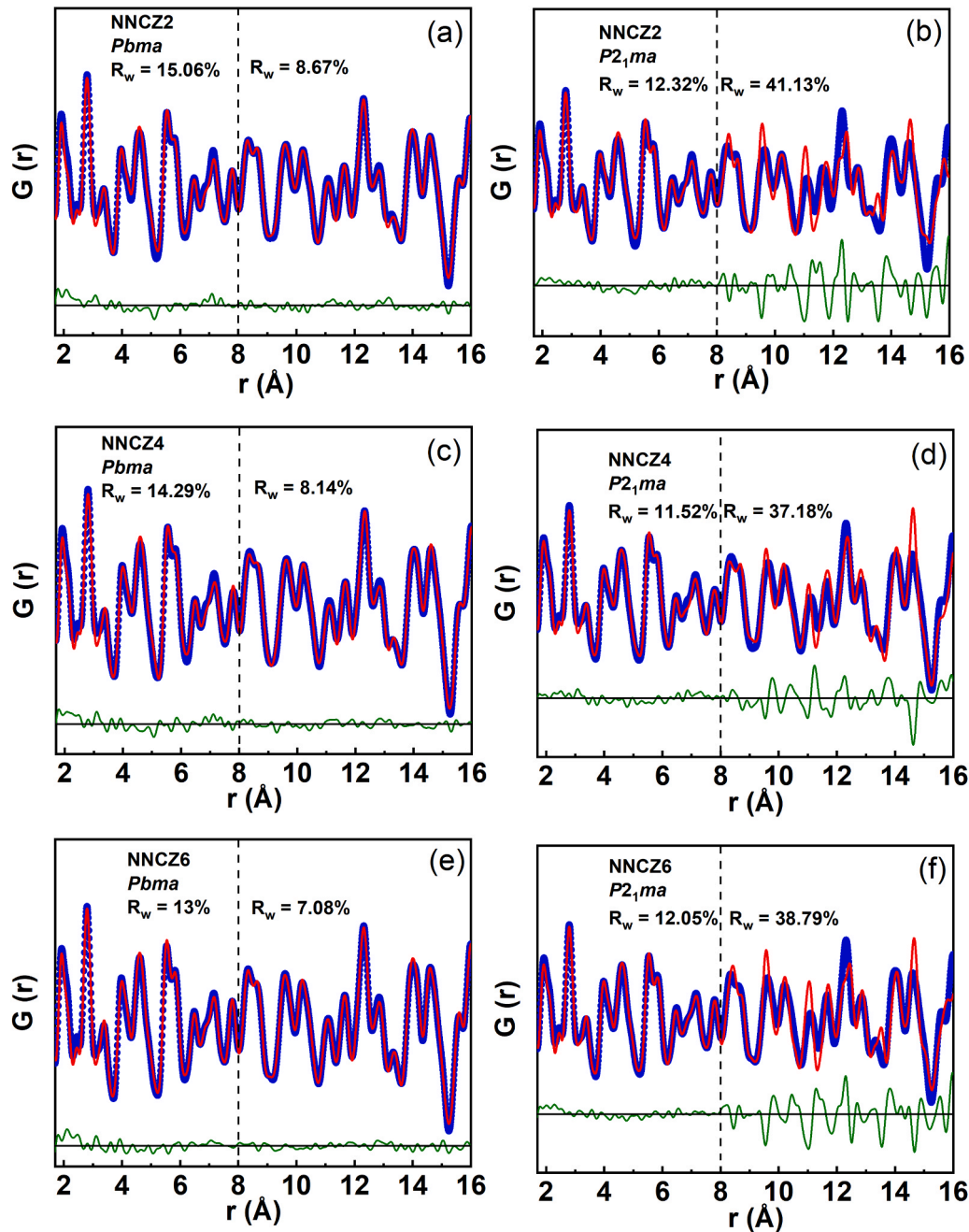
Fig. 8. Fits of neutron $G(r)$ for $(1-x)NaNbO_3-xCaZrO_3$ at room temperature using *Pbma* (AFE) and $P2_1ma$ (FE) structural symmetries for $r \sim 1.7$–16 Å. (a,b) NNCZ2, (c, d) NNCZ4, and (e,f) NNCZ6. Note that the unit cell dimensions of $P2_1ma$ and *Pbma* are approximately 8 Å and 16 Å, respectively.

local structure leads to the net displacement observed in the average *P* phase with *Pbma* structure.

4.2. Driving force for higher AFE phase fraction

The 180° twin model for the average AFE phase can be used to rationalize the variation in the FE/AFE phase fractions, as explained in our earlier publications [6]. Fig. 13 illustrates the two scenarios with different widths of the twin variants and the twin boundary regions. The twin boundary region is defined as one unit cell of the *Pbma* structure, which corresponds to ~1.6 nm along the *b* axis. In the first scenario, the width of the individual twin variants is much wider than that of the twin boundary region, which therefore yields a higher volume fraction of the average FE *Q* phase with the $P2_1ma$ structure. In the second scenario, the width of the individual twin variants is comparable to that of the twin

boundary region, which therefore yields a higher volume fraction of the average AFE *P* phase with the *Pbma* structure. Following this model, the lower value of the average *Q* phase in the heterovalent Ca/Zr doped $NaNbO_3$ results from a more extensive local twinning.

The next question is how higher Ca/Zr doping can lead to more local twinning. As we explained earlier in [6], the degree of local twinning in $NaNbO_3$ solid-solutions depends on a competition between the relative strengths of the long-range polarization field due to B(Nb)-site displacements and local non-collinear dipoles due to A(Na)-site displacements. The relative strengths of the A- and B-site centered dipoles can be gauged from the relative distortions around the A- and B-sites, which are determined from the BO_6 and AO_{12} distortion indices, *D*. The magnitude of the distortions (*D*) are calculated according to the equation
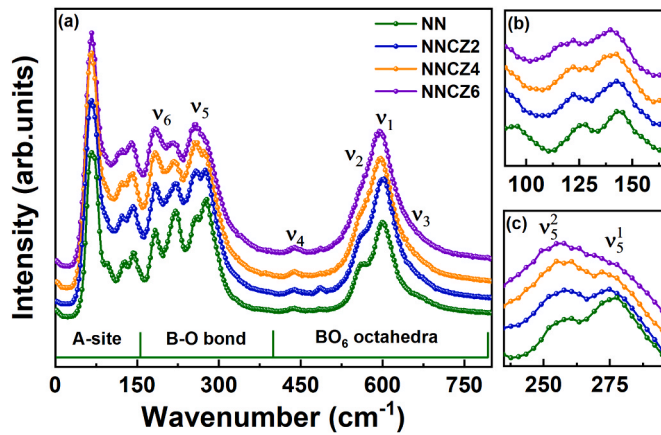
Fig. 9. (a) Raman spectra of (1-x) NaNbO$_3$-xCaZrO$_3$ measured at room temperature. NN, NNCZ2, NNCZ4, and NNCZ6 refer to x = 0, 0.02, 0.04, and 0.06, respectively. (b) shows the enlarged view of the Raman spectra in the range of 90–165 cm^{-1} and (c) shows the bending modes of BO$_6$ octahedra at 256 cm^{-1} (ν_5^2) and 278 cm^{-1} (ν_5^1).

$$D = \frac{1}{n}\left[\sum_i^n \frac{|d_i - d|}{d}\right] \qquad (5)$$

where n is the coordination number, d_i and d are the individual and average values of the different A(B) – O interatomic distances, respectively [31]. If the AO$_{12}$ distortion index is much higher than the BO$_6$ distortion index, it promotes more extensive 180° twinning of the local structure and vice-versa.

Fig. 14 shows the calculated D for the local atomic structures obtained from neutron G(r) analysis in the range of r~1.7–8 Å using the P2$_1$ma model. The P2$_1$ma model is used to calculate to obtain the site-specific distortions, since it best describes the local structure. Earlier works indicate that Zr atom displacements within the oxygen octahedra tend to be much lower as compared to ferroelectrically active ions such as Ti [32], whereas Ca ions can displace significantly within the oxygen dodecahedra due to its smaller size [33]. So presence of these dopant

ions is expected to modify the overall atomic displacements at A and B sites, when compared with respect to those in pure NaNbO$_3$. Note that the distortion values here are obtained with reference to the atomic sites, however, we do not distinguish between the displacements of Ca/Na atoms at the A-site or Nb/Zr atoms at the B-site. It can be seen that the D value for AO$_{12}$ is significantly larger than that for BO$_6$, for all the studied compositions, which is consistent with pure NaNbO$_3$ or solid-solution of K$_{0.01}$Na$_{0.99}$NbO$_3$ [6,22]. This suggests that the local distortion caused by the A-site dipoles plays a key role in creating twin domains in the Ca/Zr-doped NaNbO$_3$. However, compared to pure NaNbO$_3$, Ca/Zr-doped NaNbO$_3$ has a much higher volume fraction of the AFE P phase. We explain this due to the heterovalent nature of the Ca/Zr dopants. The introduction of additional charge disorders from the heterovalent ions weakens the long-range polarization fields, which would therefore augment the effect of the non-uniform A-site dipoles and therefore promote local twinning. Indications for this can be observed from microstructures of Ca-doped NaNbO$_3$, such as reported in [34], which shows fine-scale lamellar structure. Higher density of twin boundaries makes the local structure appear closer to *Pbma* structure and hence increase the apparent volume fraction of the average AFE P phase.

4.3. Relation of local structure to energy-storage properties

We can observe from Fig. 3 that the characteristics of the macroscopic P-E hysteresis loop changes with increased Ca/Zr doping, such as pinching of the loop near zero electric field, increase of the maximum breakdown electric field strength and higher energy storage efficiency. Correspondingly, we observe from structural measurements an increase in the percentage of the average AFE P phase with higher Ca/Zr doping. However, it is noteworthy that while both NNCZ4 (71.9%) and NNCZ6 (74.3%) compositions have similar volume fractions of the AFE phase (Fig. 5), the latter exhibits a thinner P-E loop and higher breakdown strength (200 kV/cm for NNCZ6 as compared to 180 kV/cm for NNCZ4). Therefore, the change in electrical properties of NNCZ ceramics as a function of composition cannot be fully attributed to the AFE phase percentage alone. Instead, the doping-induced changes in electrical properties can be possibly explained based on a twin model as described below.
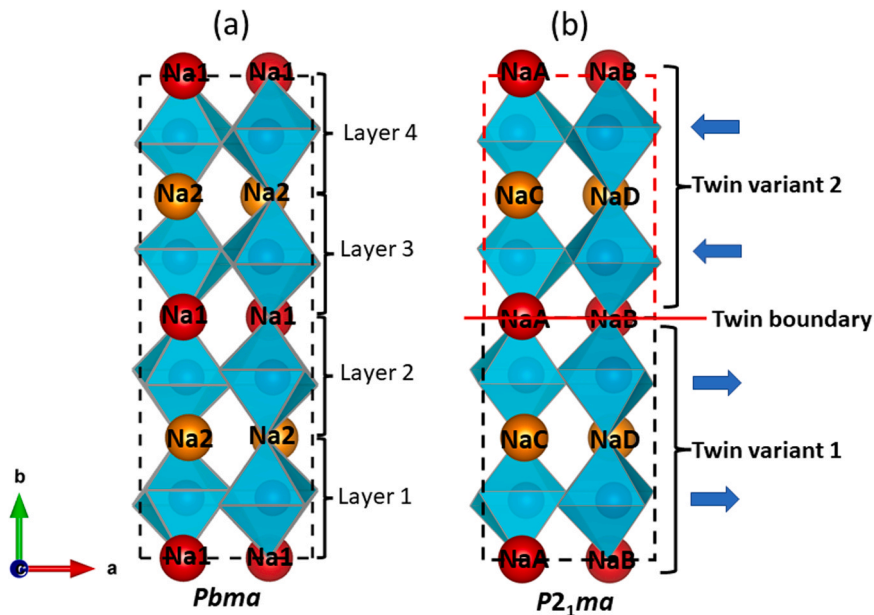
Fig. 10. Illustration of differences between (a) the *Pbma* structure (b) the *P2$_1$ma* structures. The layers 3 and 4 in the *P2$_1$ma* structure shows after 180° twinning along the b-axis. The blue arrows indicate average dipole movement directions. The red line represents the twin boundary. The unit cell of the *Pbma* and *P2$_1$ma* structures are highlighted by the dashed lines.
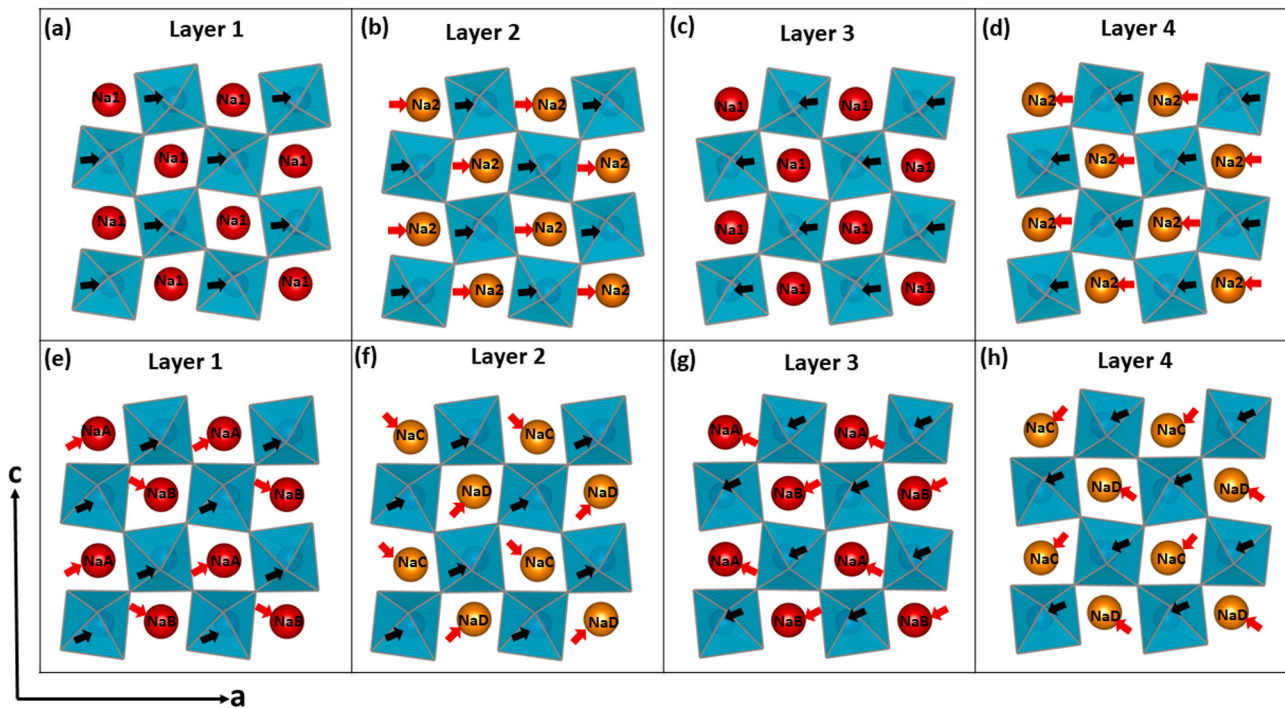
Fig. 11. Illustration of cation ions off-centering displacement in different layers: (a-d) *Pbma* structure, (e-f) $P2_1ma$ structure, (g-h) $P2_1ma$ structure after 180° twining. The arrows indicate the off-centering direction of A-site and B-site atoms. The red and orange atoms are Na1 and Na2 sites, respectively. The Nb atoms are located within the oxygen octahedra.
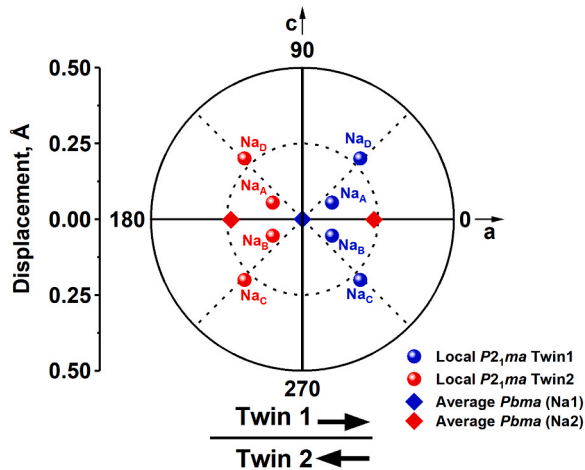
Fig. 12. Polar plot showing the direction of A-site atom displacements within individual 180° twin variants at room temperature.

Based on local atomic structural measurements, we deduce that the local atomic symmetry remains unchanged with Ca/Zr doping, while the increase in AFE *P* phase can be attributed to the formation of more 180° twin boundaries, which is furthermore accentuated by the introduction of charge disorder such as Zr'_{Nb} and Ca_{Na}. It is likely that simultaneous doping with both Ca and Zr will lead to the formation of local electrical dipoles, viz. $Zr'_{Nb} - Ca_{Na}$. Such defect dipoles can locally pin the twin boundary by associating with the dipoles of the local twin variant and increasing their switching barrier, such as illustrated in Fig. 15. The proposed model here is similar to earlier studies, which associated defect-dipole-induced pinning of polar interfaces, such as domain boundaries, with the pinching of macroscopic polarization-electric field hysteresis loops, such as refs [35,36]. For Ca/Zr-doped NN, application of a sufficiently large electric field can induce motion of the twin

boundaries between these pinning centers, which leads to change in the macroscopic polarization. However, if enough defect dipoles are present, then the twin boundaries are constrained from large scale displacements and are forced to return close to their original position upon return to zero electric field. Thus, the overall twin structure remains stable in spite of local twin boundary displacements. This can explain the pinched characteristics of the P-E loops and thinning of the hysteresis loops with higher Ca/Zr doping.

The twin model is also corroborated from other recent microscopic studies, such as [14]. Note that the substitution of Na with Ca in NaNbO$_3$ alone does not result in pinched P-E loops even though it leads to fine twin structures, since such substitution only introduces charge disorder but does not cause formation of defect dipoles [34,37]. On the other hand, simultaneous doping with Sr and Mn gives rise to pinched thin P-E hysteresis loops, which could be attributed to dipoles between Sr_{Na} and Mn'_{Nb} (or Mn''_{Nb}) [37]. Another factor to note is strong temperature dependence of electric-field-induced maximum polarization in Ca/Zr-doped NN ceramics. For example, in NNCZ4, the field-induced polarization increases by a factor of more than 10 upon increasing the temperature from RT to 120 °C [11,16], even though there is no phase transition in this temperature range. It is tempting to associate such increase in field-induced polarization to increased mobility of twin boundaries between pinning centers at higher temperatures. However, further systematic experiments on temperature dependent polarization behavior in NNCZ ceramics will be needed to investigate this matter further.

5. Conclusions

The stability of the AFE phase during electrical cycling is a critical issue for improving the energy storage capabilities of NaNbO$_3$-based ceramics. Here, we explained the microscopic mechanism for AFE-like behavior and enhanced energy storage capacity of Ca/Zr-doped NaNbO$_3$ ceramics based on their detailed structural characterization by neutron and Raman scattering experiments. Our study reveals that
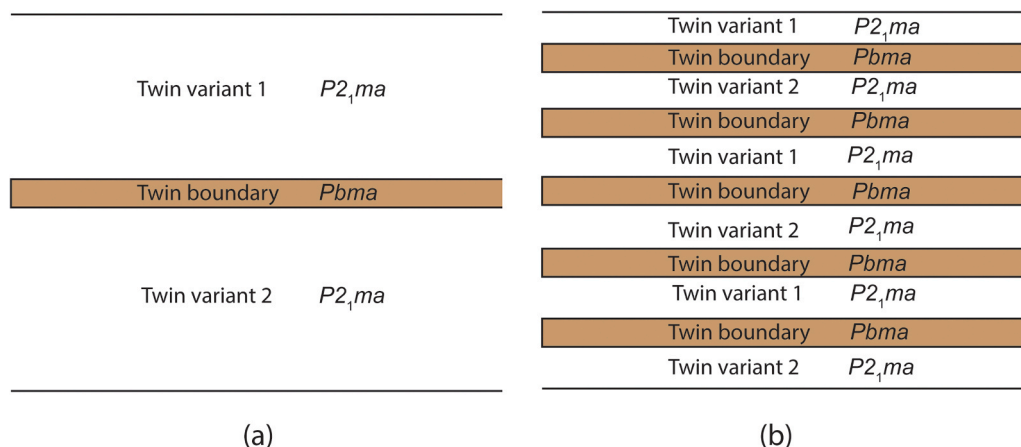
Fig. 13. Schematic representation of two possible scenarios for 180° twin structures. (a) shows a scenario with lower density of twin boundaries and hence lower average AFE phase. (b) shows a scenario with higher density of twin boundaries and hence higher average AFE phase percentage.
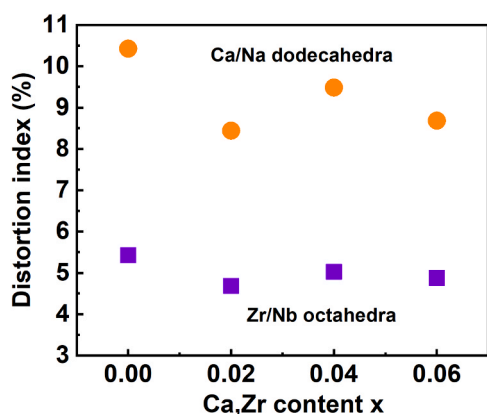
Fig. 14. AO_{12} and BO_6 distortion indices obtained from PDF refinement as a function of composition.
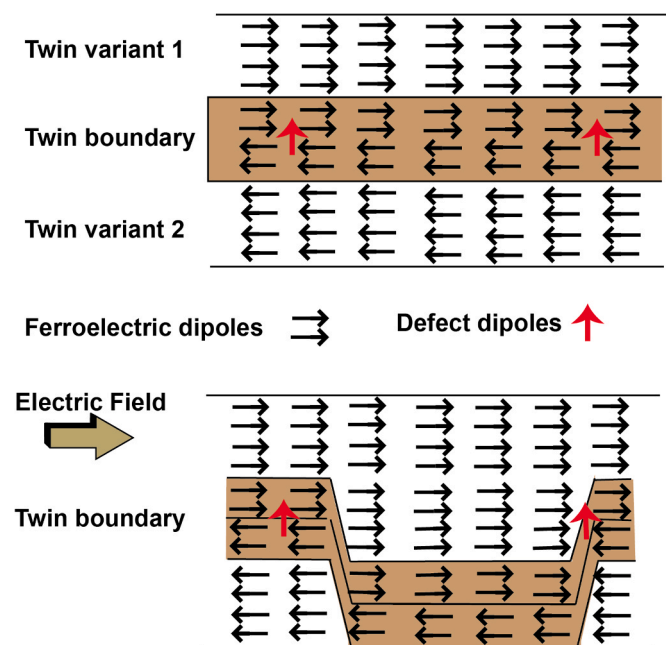
Fig. 15. Schematic illustration of 180° twin boundary motion between the pinning centers under the application of an electric field.

the introduction of heterovalent Ca/Zr dopants leads to an apparent increase in the average AFE phase, however, the local atomic configuration retains the symmetry of the FE $P2_1ma$ structure. The apparent increase in the AFE phase percentage is explained as a result of a higher density of 180° twin boundaries, which are formed due to the introduction of microscopic charge disorder. Furthermore, we assert that the stability of the AFE-like behavior during electrical cycling in Ca/Zr-doped $NaNbO_3$ is principally due to the pinning of the twin boundaries by defect dipoles, viz. $Zr'_{Nb} - Ca_{Na}$, rather than due to an increase in the AFE crystallographic phase. These insights will help towards more rational design of Pb-free antiferroelectric materials for high-power energy storage applications.

CRediT authorship contribution statement

Cho Sandar Htet: Investigation, Formal analysis, Methodology, Writing – original draft, Visualization; **Alicia Manjon-Sanz, Jue Liu, Chaimae Babori, Mahmoud Barati, Frederick P. Marlton**: Investigation, Methodology, Writing – review and editing; **Laurent Daniel, Mads Ry Vogel Jorgensen**: Writing – review and editing; **Abhijit Pramanick**: Conceptualization, Project administration, Writing – review and editing.

Declaration of Competing Interest

The authors declare that they have no known competing financial interests or personal relationships that could have appeared to influence the work reported in this paper.

Appendix A. Supporting information

Supplementary data associated with this article can be found in the online version at doi:10.1016/j.jeurceramsoc.2023.10.072.

References

[1] C.A. Randall, Z. Fan, I. Reaney, L.Q. Chen, S. Trolier-McKinstry, Antiferroelectrics: history, fundamentals, crystal chemistry, crystal structures, size effects, and applications, J. Am. Ceram. Soc. 104 (8) (2021) 3775–3810.

[2] N. Luo, K. Han, M.J. Cabral, X. Liao, S. Zhang, C. Liao, G. Zhang, X. Chen, Q. Feng, J.-F. Li, Constructing phase boundary in $AgNbO_3$ antiferroelectrics: pathway simultaneously achieving high energy density and efficiency, Nat. Commun. 11 (1) (2020) 4824.

[3] Q. Zhang, S. Jiang, Y. Zeng, M. Fan, G. Zhang, Y. Zhang, Y. Yu, J. Wang, J. He, Large electric-induced pyroelectric properties in $(Pb_{0.87}La_{0.02}Ba_{0.1})(Zr_{0.7}Sn_{0.24}Ti_{0.06})O_3$ antiferroelectric ceramics with excess PbO, J. Appl. Phys. 109 (12) (2011), 124111.

[4] Z. Liu, T. Lu, F. Xue, H. Nie, R. Withers, A. Studer, F. Kremer, N. Narayanan, X. Dong, D. Yu, Lead-free $(Ag, K)NbO_3$ materials for high-performance explosive energy conversion, Sci. Adv. 6 (21) (2020), eaba0367.

[5] C. Kittel, Theory of antiferroelectric crystals, Phys. Rev. 82 (5) (1951) 729.

[6] C.S. Htet, A.M. Manjón-Sanz, J. Liu, J. Kong, F.P. Marlton, S. Nayak, M.R. V. Jørgensen, A. Pramanick, Effect of local structural distortions on antiferroelectric–ferroelectric phase transition in dilute solid solutions of $K_xNa_{1-x}NbO_3$, Inorg. Chem. 61 (50) (2022) 20277–20287.

[7] M.D. Peel, S.E. Ashbrook, P. Lightfoot, Unusual phase behavior in the piezoelectric perovskite system, $Li_xNa_{1-x}NbO_3$, Inorg. Chem. 52 (15) (2013) 8872–8880.

[8] H. Qi, R. Zuo, Evolving antiferroelectric stability and phase transition behavior in $NaNbO_3$-$BaZrO_3$-$CaZrO_3$ lead-free ceramics, J. Eur. Ceram. Soc. 39 (7) (2019) 2318–2324.

[9] H. Guo, H. Shimizu, Y. Mizuno, C.A. Randall, Strategy for stabilization of the antiferroelectric phase (Pbma) over the metastable ferroelectric phase ($P2_1ma$) to establish double loop hysteresis in lead-free $(1-x)NaNbO_3$-$xSrZrO_3$ solid solution, J. Appl. Phys. 117 (21) (2015), 214103.

[10] M.-H. Zhang, N. Hadaeghi, S. Egert, H. Ding, H. Zhang, P.B. Groszewicz, G. Buntkowsky, A. Klein, J. Koruza, Design of lead-free antiferroelectric $(1–x)NaNbO_3–x$ $SrSnO_3$ compositions guided by first-principles calculations, Chem. Mater. 33 (1) (2020) 266–274.

[11] H. Shimizu, H. Guo, S.E. Reyes-Lillo, Y. Mizuno, K.M. Rabe, C.A. Randall, Lead-free antiferroelectric: $xCaZrO_3$-$(1-x)NaNbO_3$ system ($0 \le x \le 0.10$), Dalton Trans. 44 (23) (2015) 10763–10772.

[12] J. Ye, G. Wang, X. Chen, F. Cao, X. Dong, Enhanced antiferroelectricity and double hysteresis loop observed in lead-free $(1-x)NaNbO_3$-$xCaSnO_3$ ceramics, Appl. Phys. Lett. 114 (12) (2019), 122901.

[13] L. Gao, H. Guo, S. Zhang, C.A. Randall, A perovskite lead-free antiferroelectric $xCaHfO_3$-$(1-x)NaNbO_3$ with induced double hysteresis loops at room temperature, J. Appl. Phys. 120 (20) (2016), 204102.

[14] N. Luo, L. Ma, G. Luo, C. Xu, L. Rao, Z. Chen, Z. Cen, Q. Feng, X. Chen, F. Toyohisa, Y. Zhu, J. Hong, J.-F. Li, S. Zhang, Well-defined double hysteresis loop in $NaNbO_3$ antiferroelectrics, Nat. Commun. 14 (1) (2023), 1776.

[15] H. Guo, H. Shimizu, Y. Mizuno, C.A. Randall, Domain configuration changes under electric field-induced antiferroelectric-ferroelectric phase transitions in $NaNbO_3$-based ceramics, J. Appl. Phys. 118 (5) (2015), 054102.

[16] Z. Liu, J. Lu, Y. Mao, P. Ren, H. Fan, Energy storage properties of $NaNbO_3$-$CaZrO_3$ ceramics with coexistence of ferroelectric and antiferroelectric phases, J. Eur. Ceram. Soc. 38 (15) (2018) 4939–4945.

[17] Mel I. Mendelson, Average grain size of polycrystalline ceramics, J. Am. Ceram. Soc. 52 (1969) 443.

[18] V. Segouin, M. Domenjoud, Y. Bernard, L. Daniel, Mechanics-aided digital image correlation for the investigation of piezoelectric and ferroelectric behaviour of a soft PZT, J. Eur. Ceram. Soc. 39 (6) (2019) 2091–2102.

[19] A. Huq, M. Kirkham, P.F. Peterson, J.P. Hodges, P.S. Whitfield, K. Page, T. Hűgle, E.B. Iverson, A. Parizzi, G. Rennich, POWGEN: rebuild of a third-generation powder diffractometer at the Spallation Neutron Source, J. Appl. Crystallogr. 52 (5) (2019) 1189–1201.

[20] B.H. Toby, R.B. Von Dreele, GSAS-II: the genesis of a modern open-source all purpose crystallography software package, J. Appl. Crystallogr. 46 (2) (2013) 544–549.

[21] S. Mishra, R. Mittal, V.Y. Pomjakushin, S. Chaplot, Phase stability and structural temperature dependence in sodium niobate: a high-resolution powder neutron diffraction study, Phys. Rev. B 83 (13) (2011), 134105.

[22] C.S. Htet, S. Nayak, A. Manjón-Sanz, J. Liu, J. Kong, D. Sørensen, F. Marlton, M. Jørgensen, A. Pramanick, Atomic structural mechanism for ferroelectric-antiferroelectric transformation in perovskite $NaNbO_3$, Phys. Rev. B 105 (17) (2022), 174113.

[23] L. McCusker, R. Von Dreele, D. Cox, D. Louër, P. Scardi, Rietveld refinement guidelines, J. Appl. Crystallogr. 32 (1) (1999) 36–50.

[24] T. Proffen, S. Billinge, T. Egami, D. Louca, Structural analysis of complex materials using the atomic pair distribution function—A practical guide, Z. für Krist. -Cryst. Mater. 218 (2) (2003) 132–143.

[25] D.A. Keen, A comparison of various commonly used correlation functions for describing total scattering, J. Appl. Crystallogr. 34 (2) (2001) 172–177.

[26] C. Farrow, P. Juhas, J. Liu, D. Bryndin, E. Božin, J. Bloch, T. Proffen, S. Billinge, PDFfit2 and PDFgui: computer programs for studying nanostructure in crystals, J. Phys.: Condens. Matter 19 (33) (2007), 335219.

[27] R. Shakhovoy, S. Raevskaya, L. Shakhovaya, a.D. Suzdalev, I. Raevski, Y.I. Yuzyuk, A. Semenchev, M. El Marssi, Ferroelectric Q and antiferroelectric P phases' coexistence and local phase transitions in oxygen-deficient $NaNbO_3$ single crystal: micro-Raman, dielectric and dilatometric studies, J. Raman Spectrosc. 43 (8) (2012) 1141–1145.

[28] A. Xie, H. Qi, R. Zuo, A. Tian, J. Chen, S. Zhang, An environmentally-benign $NaNbO_3$ based perovskite antiferroelectric alternative to traditional lead-based counterparts, J. Mater. Chem. C 7 (48) (2019) 15153–15161.

[29] Y. Ye, A. Cui, L. Gao, K. Jiang, L. Zhu, J. Zhang, L. Shang, Y. Li, G. Wang, X. Dong, In situ Raman scattering studies of pressure-temperature phase diagrams in antiferroelectric $xCaSnO_3$-modified $NaNbO_3$ ceramics, Appl. Phys. Lett. 119 (13) (2021), 132905.

[30] R. Jiménez, M. Sanjuan, B. Jiménez, Stabilization of the ferroelectric phase and relaxor-like behaviour in low Li content sodium niobates, J. Phys.: Condens. Matter 16 (41) (2004) 7493.

[31] W. Baur, The geometry of polyhedral distortions. Predictive relationships for the phosphate group, Acta Crystallographica Section B: Structural Crystallography and Crystal, Chemistry 30 (5) (1974) 1195–1215.

[32] A. Akbarzadeh, S. Prosandeev, E.J. Walter, A. Al-Barakaty, L. Bellaiche, Finite-temperature properties of $Ba(Zr, Ti)O_3$ relaxors from first principles, Phys. Rev. Lett. 108 (25) (2012), 257601.

[33] D. Fu, M. Itoh, S.-y Koshihara, T. Kosugi, S. Tsuneyuki, Anomalous phase diagram of ferroelectric $(Ba, Ca)TiO_3$ single crystals with giant electromechanical response, Phys. Rev. Lett. 100 (22) (2008), 227601.

[34] B. Liu, X. Tan, Structure, ferroelectric, and dielectric properties of $(Na_{1-2x}Ca_x)NbO_3$ ceramics, J. Mater. Res. 36 (2021) 1076–1085.

[35] P.V. Lambeck, G.H. Jonker, The nature of domain stabilization in ferroelectric perovskites, J. Phys. Chem. Solids 47 (1986) 453–461.

[36] G. Robert, D. Damjanovic, N. Setter, Preisach modeling of ferroelectric pinched loops, Appl. Phys. Lett. 77 (2000) 4413–4415.

[37] M.-H. Zhang, H. Ding, S. Egert, C. Zhao, L. Villa, L. Fulanović, P.B. Groszewicz, G. Buntkowsky, H.-J. Kleebe, K. Albe, A. Klein, J. Koruza, Tailoring high-energy storage $NaNbO_3$-based materials from antiferroelectric to relaxor states, Nat. Commun. 14 (1) (2023), 1525.